ACCSCIENCE PUBLISHING

International Journal of Bioprinting

RESEARCH ARTICLE

Development of P(3HB-co-3HHx) nanohydroxyapatite (nHA) composites for scaffolds manufacturing by means of fused deposition modeling

Juan Ivorra-Martinez[1]*, Ines Ferrer[2], Roberto Aguado[3], Marc Delgado-Aguilar[3], Maria Luisa Garcia-Romeu[2], and Teodomiro Boronat[1]

[1]Technological Institute of Materials (ITM), Universitat Politècnica de València (UPV), Plaza Ferrándiz y Carbonell 1, 03801 Alcoy, Spain

[2]Department of Mechanical Engineering and Industrial Construction, University of Girona, c/M. Aurèlia Campmany, 61, Girona 17071, Spain

[3]LEPAMAP-PRODIS Research Group, University of Girona, c/M. Aurèlia Campmany, 61, Girona 17071, Spain

(This article belongs to the *Special Issue: Novel Materials and Processing for Medical 3D Printing and Bioprinting*)

Abstract

This work reports on the development of nanocomposites based on poly(3-hydroxybutyrate-*co*-3-hydroxyhexanoate) [P(3HB-*co*-3HHx)] and nanohydroxyapatite (nHA) for the development of scaffolds by means of a two-stage extrusion process followed by a 3D printing process. Tensile test samples were produced for the characterization of the materials. Each processing thermal cycle promoted a slight thermal degradation, identified by means of differential scanning calorimetry (DSC) and thermogravimetric analysis (TGA). Also, a viscosity reduction was observed in the rheological measurements. The 3D-printed tensile test samples exhibited increasing stiffness at increasing nHA content (with elastic modulus values close to 1000 MPa), while tensile strength and strain at break were reduced. Nonetheless, the deposition direction oriented with the tensile direction (raster angle of 0°C) exhibited the highest tensile strength (18 MPa) but lower elongation at break than the 45°/–45°C deposition, which resulted in the highest strain (up to 17%). Regarding the scaffolds, they were degraded in phosphate-buffered saline at 37°C for 8 weeks. This degradation was identified by a reduction of their weight (between 1.5% and 3.0%) and reduced mechanical behavior measured by means of a compression test. Scaffolds showed a decrease of the compression strength (from values close to 13 MPa to 9 MPa).

Keywords: Hydroxyapatite; Polyhydroxyalkanoates; Fused filament deposition modeling; Additive manufacturing; Scaffold

***Corresponding author:**
Juan Ivorra-Martinez
(juaivmar@doctor.upv.es)

Citation: Ivorra-Martinez J, Ferrer I, Aguado R, Delgado-Aguilar M, Garcia-Romeu ML, Boronat T. Development of P(3HB-co-3HHx) nanohydroxyapatite (nHA) composites for scaffolds manufacturing by means of fused deposition modeling. *Int J Bioprint*. 2024;10(1):0156. doi: 10.36922/ijb.0156

Received: May 07, 2023
Accepted: June 16, 2023
Published Online: August 24, 2023

1. Introduction

Additive manufacturing has been developed as a novel manufacturing methodology. Some of the main advantages of additive manufacturing are the freedom it provides toward design, mass customization, and manufacture of complex structures, as well as rapid prototyping.[1] Among the different additive manufacturing techniques, including stereolithography (SLA), selective laser sintering (SLS), contour crafting (CC), powder bed fusion (PBF), or fused deposition modeling (FDM), the latter has evolved over the recent years to the point that it is currently applied in different sectors, such as construction, automotive, and biomedicine.[2-5] The emergence of FDM, which is also known as 3D printing, has positively affected the medical industry, particularly due to its ability in producing customized prostheses, scaffolds for tissue regeneration or even highly efficient drug delivery systems.[6,7] Unlike conventional processes like casting, forging or machining operations imply high manufacturing costs for low-volume production series. Additive manufacturing is advantageous in terms of customization, as multiple operations and production processes can be avoided. For instance, production of item with complex geometries can even be clearly simplified when additive manufacturing is used.[8] This is because of the layer-by-layer operation principle, which allows building up the final product based on the geometry obtained by means of computer-aided design (CAD) software.[9,10]

Among the different healthcare applications, in which FDM can be used, the fabrication of scaffolds for tissue engineering is one of the most interesting ones. A clear example is the production of nanohydroxyapatite (nHA)-polylactic acid (PLA) scaffolds, which have been reported to benefit the reconstruction of large bone defects,[11] as they enhance the adhesion and proliferation of cells to carry out the regeneration process of damaged tissue.[12,13] Indeed, one of the most important features in optimizing scaffold performance is obtaining successfully interconnected pores to promote nutrient transport and integration with surrounding tissue.[14-16]

The development of medical devices can be satisfied by several materials, including metals (i.e., cobalt-chrome alloys or titanium), ceramic materials, and polymers and polymer-based composites.[17] Each kind of material has different properties; therefore, the final application of medical device depends on the material employed. Metallic materials have been historically used for medical implants due to their biocompatibility in the long term and high wear resistance, which allow their use in artificial joints, stents, or valves.[18,19] Ceramic materials, such as hydroxyapatite (HA) and tricalcium phosphate (TCP), are attracting interest in the medical sector due to their presence in bones, although its use is limited by their intrinsic fragility. Indeed, this limits its application as bulk material, and most of the works have reported their use as prosthesis coating or filler.[11,13,20,21] Concretely, HA constitutes around the 70% by weight of the human bones and possesses great osteoconductive capacity, so it has been used in different applications in the field of tissue engineering, particularly in bone regeneration.[22] However, its powder-like structure and rigidity limit its application as bulk material, requiring the use of a polymer like PLA to be embedded into during the processing stage.[21,23-25] Among the matrices, thermoplastic materials deserve special attention, as they are mostly used in FDM. Polymers derived from fossil resources such as polyethylene (PE) have been broadly used in producing implants used in applications such as implants. However, polymers obtained from renewable resources are also widely used in FDM, such as polylactic acid (PLA), poly(lactic-co-glycolic acid) (PLGA), or polyhydroxyalkanoates (PHAs).[5,11,26-29] Furthermore, biodegradable, oil-based, and compatible polymers are also attracting interest, particularly in combination with bio-based and biodegradable materials, as it is the case of polycaprolactone (PCL).[30] In the broad range of bio-sourced polymers, PHAs are gaining interest due to their compatibility, as some of their constituents can be naturally found in human blood,[27] making them an excellent option for medical devices.[29,31]

Apart from biocompatibility, which is a requirement for any medical device, the degradation rate of materials is also a parameter to be considered, particularly for temporary implants and scaffolds that would require a second intervention for an after-use removal.[32] The degradation process of polymers within the human body is critical, and some polymers may generate inflammation, as is the case with PLGA.[33] For instance, the oligomers released from PLA degradation have been reported to produce toxicity within the human body due to lactic acid accumulation. On the other hand, the 3-hydroxybutyrate (3HB) that is produced from PHA degradation is a common metabolite in living species due to the breakage of long-chain fatty acids, meaning that PHA is biocompatible in degradation conditions.[34-36] Indeed, the inflammatory response of PLA compared to "poly(3-hydroxybutyrate-co-3-hydroxyhexanoate [P(3HB-*co*-3HHx)]" has been previously reported to be more intense.[37] Among the different PHAs, poly(3-hydroxybutyrate) (PHB) is the most common one, but its thermal stability is low and thus, it often degrades during processing since its processing temperature is close to the temperature at the beginning of degradation, leading to a narrow processing window.[38] Copolymers such as P(3HB-*co*-3HHx) can achieve higher thermal stability that allows for a wider processing window, making its processability more suitable by means of additive manufacturing in comparison with other PHA.[39]

The use of composite materials opens a new paradigm, as the combination of two or more materials may result in interesting properties. For instance, the combination of polymers with ceramic fillers (e.g., HA) can confer

Table 1. P(3HB-*co*-3HHx) characteristics according to the supplier

Characteristic	Value	Units	Standard
Melt flow index (MFI)	1	g/10 min	ISO 1133-2 (160°C and 2.16 kg)
Density	1.20	g/cm^3	ISO 1183-1
Melting temperature	124	°C	ISO 11357
Glass transition temperature (T_g)	1	°C	ISO 11357
Young's modulus	0.9	GPa	EN ISO 527
Strain at break	21	%	EN ISO 527
Vicat	62	°C	ISO 1133-5

biocompatibility and bone regeneration capacity to the neat polymer. From the mechanical point of view, ceramic materials can act as a reinforcement, leading to an increase of stiffness of the polymer composite. In addition, the composites are more ductile than the ceramic material.[40] Of note, increasing HA contents in PLA resulted in higher biocompatibility and bioactivity of PLA, or cell proliferation enhancement in the case of PCL as matrix.[41,42]

The development of scaffold structures for bone regeneration process is a current trend, and different kinds of studies have been carried out to improve bone regeneration process.[43] During the healing process, blood and cells can penetrate the porous structure in order to start bone formation.[44] Depending on the manufacturing technique employed for the obtention of the scaffold, different properties will be obtained. As Eltom *et al.* propose, scaffolds were conventionally manufactured by freeze-drying, solvent casting, gas foaming, electrospinning, or thermal-induce phase separation, but with the grow of additive manufacturing techniques, different approaches have been made to develop scaffolds with rapid prototyping techniques.[45] In this sense, the development of scaffolds made by FDM has been conducted in different polymeric matrix like PLA, PCL, and also P(3HB-*co*-3HHx).[23,39,46] In addition, the combination of biopolymers with ceramic fillers to enhance the tissue regeneration has been investigated.[47,48] In most cases, only the cell adhesion over the scaffold is studied but in some cases, the study of the mechanical performance of the scaffold is also conducted.[49]

The main aim of this work is the development of nanocomposites prepared from P(3HB-*co*-3HHx) and nHA, targeting the development of bioactive and biodegradable materials for 3D printing of medical devices. In this work, standard tensile specimens with 100% infill and different infill directions were 3D-printed to assess the mechanical properties of the developed nanocomposites. In addition, the effect of all the processing stages was analyzed by thermal tests, such as differential scanning calorimetry (DSC) and thermogravimetry analysis (TGA), to measure the changes in enthalpy and main characteristic temperatures. In addition, rheological studies were performed to measure the viscosity changes in each processing stage. The main novelty focuses on the assessment of the changes that take place during a hydrolytic degradation process of the material. In this sense, different studies have been conducted by other authors that measure the cell adhesion, but the effect on the physical properties over the immersion time has not been deeply investigated. In this case, scaffolds were fabricated and immersed in phosphate-buffered saline (PBS) at 37°C up to 8 weeks. To monitor the changes that took place during the immersion, compression mechanical properties, changes in the weight of the sample and changes in the pH of the medium were measured.

2. Materials and methods

2.1. Materials

Commercial-grade P(3HB-*co*-3HHx) (Ercros® PH 110) supplied by Ercros S.A. (Barcelona, Spain) in pellet form (cylindrical shape with an average of 3 mm length and 2 mm diameter) were used as polymer matrix of the nanocomposites. The main characteristics of the polymer, according to the supplier, are reported in Table 1. Commercially available nHA, purchased from Merck (Madrid, Spain) (Ref: 677418) was used as filler for the nanocomposites. According to the supplier, this nHA has a surface area of higher than 9.4 m^2/g, as determined by Brunauer–Emmet–Teller (BET) analysis, and a molecular weight of 502.31 g/mol. The particle size was lower than 200 nm and the purity was reported to be equal to or higher than 97%. The employed material is a polymer with low melt flow index (MFI), so the temperature profile and screw speed must be adjusted properly in order to obtain a good-quality filament. Other authors have reported the employment of polymers with MFI values close to the one employed in this study.[50,51]

2.2. Preparation of nanocomposites

The matrix and the filler were dried at 80°C in an air-circulating oven (Industrial Marsé, S.A., Barcelona, Spain) for 24 h. Subsequently, the correct amount of each material was manually premixed in zippered bags at nHA contents of 0.0, 2.5, 5.0, and 10.0 wt%. The premixture consisted of 800 g of material, which were passed through a twin-screw extruder (Dupra S.L., Castalla, Spain) with an average residence time of 2 min. The extruder is equipped with four individual heating zones and two screws with a diameter of 25 mm and a length-to-diameter (L/D) ratio of 24. All extrusions were performed with a screw speed ranging from 20 to 25 rpm with a temperature profile of 140/145/150/155°C. This extruder was employed in order to obtain a proper filler dispersion in the polymer matrix, as the second extruder employed is a single-screw extruder designed for filament fabrication only.

The extruded materials were pelletized in an air-knife unit and stored in hermetic plastic bags to prevent moisture uptake. The resulting samples were labeled as P(3HB-*co*-3HHx)/HA content. For instance, the sample containing 5.0 wt% of nHA was codified as P(3HB-*co*-3HHx)/5HA, while the neat matrix (0.0 wt% nHA) was named as P(3HB-*co*-3HHx).

2.3. Filament extrusion and 3D printing parameters

Once the nanocomposites were prepared and pelletized, a single-screw extruder equipped with four heating zones, Next 1.0 model from 3devo (Utrecht, The Netherlands), was used to obtain the 3D printing filaments with the proper dimensions. The temperature profile from the inlet hopper to the nozzle was 150/155/160/150°C, with an extrusion speed of 5 rpm. The extruder uses a feedback cascade controller to adjust the rotational speed of the spool to target the desired filament diameter. The diameter was set at 2.85 mm, obtaining average diameters of 2.85 ± 0.03, 2.85 ± 0.05, 2.85 ± 0.04, and 2.84 ± 0.10 mm, for the nanocomposites containing 0.0, 2.5, 5.0, and 10.0 wt% of nHA, respectively. Changes in the diameters and deviation obtained for each material led to the differences in rheological behavior with the addition of the nHA. But in any cases, the filaments obtained could be perfectly employed for the manufacturing process.

3D printing was carried out using an Ultimaker 3 (Utrecht, The Netherlands) equipped with a 0.8-mm nozzle. For the present work, two geometries were considered: tensile test specimens (Figure 1a), according to ISO 527, and scaffolds of 12 × 12 × 25 mm^3 (Figure 1b). The printing parameters are given in Table 2. Figure 1 shows the geometry and raster angle of the printed materials, both for tensile test specimens (Figure 1a) and scaffolds (Figure 1b).

Three replicates were printed for each raster angle condition in the case of tensile test specimens, while 15 scaffolds were printed. For the scaffold manufacture, a cube with the mentioned external dimensions of the device was designed using FreeCAD software. To achieve the desired porosity, the gcode was set with a linear infill patter with the lines oriented at 0°/90° (with no walls and no top/bottom layers) and a 70% infill density. The infill density was chosen in order to get connected pores but with a low porosity values so that the mechanical properties were not greatly reduced.[52]

Table 2. Printing parameters for the tensile test specimens and the scaffolds

Printing process parameter	Tensile test specimens	Scaffolds
Printing temperature (°C)	170	170
Bed temperature (°C)	65	65
Printing speed (mm/s)	30	30
Layer height (mm)	0.2	0.2
Infill (%)	100	70
Raster angle (°)	0; 0/90 and 45/−45	0/90
Printing orientation	Flat	Flat

On the one hand, tensile tests were used to characterize the mechanical properties of the proposed formulations obtained by means of additive manufacturing. For this reason, an infill density of 100% was employed. Only the infill pattern was changed since it is the most relevant parameter in terms of mechanical properties in additive manufacturing.[53] Other printing parameters like the layer height were set to improve the final properties according to the information obtained in literature.[54] On the other hand, scaffolds were used to assess their degradation in a phosphate-buffered solution by means of immersion. Compression tests were also carried out with the scaffolds at a different immersion time.

2.4. Physical and mechanical characterization of nanocomposites

For the tensile test, 3D-printed standardized tensile test samples were employed following the ISO 527. For the scaffold characterization, a compression test was performed following the ISO 604. To this effect, a universal testing machine (under tensile or compression mode) ELIB 30 from S.A.E. Ibertest (Madrid, Spain) was employed. In both cases, the machine was equipped with a 5-kN load cell and a crosshead speed of 5 mm/min was selected according to the testing speeds proposed in the standard. Regarding the tensile test, three specimens of each material were tested for the raster angle proposed. In contrast, three scaffolds were tested each week for the material considered; therefore, 15 scaffolds were printed for each material. For the result analysis, on the one hand, the data recorded during tensile test were the maximum tensile strength measured during the test (tensile strength), the maximum elongation of the sample achieved during the test (elongation at break), and the tensile modulus

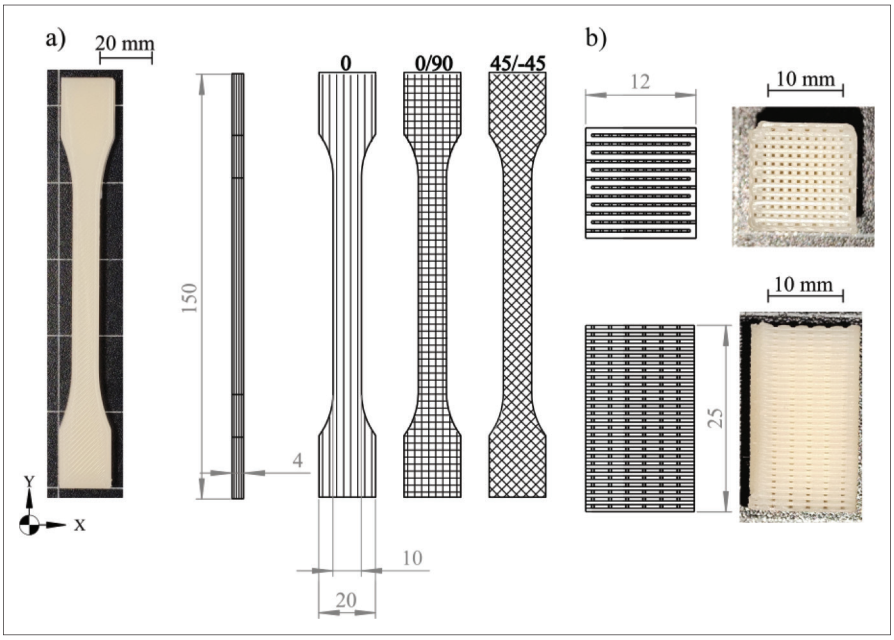

Figure 1. Geometries employed in this work: (a) tensile test specimens with different raster angles and (b) scaffolds.

from the slope of the tensile test curve. On the other hand, compression test values were taken from the yield point (the point where the curve starts to decrease) to obtain the stress at yield point and the deformation at yield point.

DSC tests were performed over a pellet obtained from the dual screw extruding process before the filament fabrication (E), a small piece from the obtained filament (F), and a small piece of a 3D-printed sample (3D) in a Mettler Toledo 821 from Mettler-Toledo Inc. (Schwerzenbach, Switzerland). First, a heating-cooling cycle was performed to remove the thermal history of the material by means of heating from 30°C to 200°C and cooling down to −40°C. The third heating scan went from −40°C to 200°C. Heating and cooling rates were set at 10°C/min, using a nitrogen atmosphere with a flow rate of 66 mL/min. The DSC test provided the melting temperature (T_m), the cold crystallization temperature (T_{cc}), the melting enthalpy (ΔH_m), and the cold crystallization enthalpy (ΔH_{cc}). Crystallinity was calculated from the enthalpies, the mass fraction of hydroxyapatite (w) and the normalized enthalpy values (ΔH_m^0), as reported in Equation I.

$$\chi_c(\%) = \frac{\Delta H_m - \Delta H_{cc}}{\Delta H_m^0 \bullet (1-w)} \times 100 \quad \text{(I)}$$

The ΔH_m^0 values for a theoretical pure crystalline P(3HB-*co*-3HHx) were noted as 146 J/g.[55]

TGA was performed using samples with an average weight of 15–25 mg in a PT1000 from Linseis (Selb, Germany). The nanocomposites were placed in 70-µL alumina crucibles and subjected to a heating from 30°C to 700°C. The heating rate was set at 20°C/min, and the tests were performed in a nitrogen atmosphere.

For the rheological measurements, cylinders with 25-mm diameter and 1-mm height after each processing stage [dual screw extruding (E), filament (F) and 3D-printed sample (3D)] were obtained for rheological measurements by means of compression molding in a hot-plate press at 160°C and 300 bar for 1 min. The rheological behavior was measured in an oscillatory rheometer AR G2 from TA Instruments (New Castle, USA). The rheometer configuration was plate-plate (diameter of 25 mm) using a gap of 0.5 mm to allow the sample insertion. Frequency sweep experiments were carried out at a fixed strain of 0.1%. The storage modulus (G′), loss modulus (G″), and the complex viscosity (η*) were determined from rheological measurements. The angular frequencies were swept from 100 to 0.01 Hz with five points per decade at 170°C.

2.5. Characterization of scaffolds

Prior to immersion in the PBS, scaffolds were numbered and weighed to obtain the initial mass (W_0). The scaffolds were then placed in individual bottles containing PBS and kept at 37°C for 8 weeks. The PBS was replaced every week, and three scaffolds were taken out every 2 weeks for characterization purposes.

The total porosity of scaffolds was determined by gravimetry according to Equation II, where $\rho_{scaffold}$ is the density of the scaffold calculated from the apparent volume and the scaffold weight, and $\rho_{material}$ is the density of each nanocomposite, which was determined in a densitometer from Testing Machines Inc. (Delaware, USA) with a resolution of 0.01 g/cm³.[56]

$$\text{Total porosity} = 1 - \frac{\rho_{\text{scafold}}}{\rho_{\text{material}}} \quad \text{(II)}$$

Scaffolds were manually dried with paper for a short period of time (less than 2 min) to remove the PBS from the surface and weighed (W_w) to obtain the amount of absorbed PBS (W_g), according to Equation III. After this, samples were oven-dried (60°C for 48 h) to remove moisture and then weighed (W_d), allowing the determination of weight loss (W_l), according to Equation IV. In each extraction, the pH of PBS was measured.

$$W_g(\%) = \frac{W_w - W_0}{W_0} \times 100 \quad \text{(III)}$$

$$W_l(\%) = \frac{W_d - W_0}{W_0} \times 100 \quad \text{(IV)}$$

Surface morphology of the scaffolds (prior and after immersion in PBS) was assessed by means of field emission scanning electron microscopy (FE-SEM) in a Zeiss Ultra 55 FESEM microscope from Oxford Instruments (Abingdon, UK), operating at an accelerating voltage of 2 kV. Samples were coated with gold-palladium alloy in an EMITECH model. SC7620 sputter coater was obtained from Quorun Technologies Ltd. (East Sussex, UK). This test was conducted to measure the mineralization ability of the different composites manufactured following the procedure proposed by Monshi *et al.*[57]

Finally, the chemical analysis of the scaffold surface was analyzed by attenuated total reflectance-Fourier transform infrared spectroscopy (ATR-FTIR). Bruker S.A. Vector 22 (Madrid, Spain) coupled with an ATR measuring accessory from Pike Technologies (Madision, WI, USA) was employed. Wavelengths between 4000 cm^{-1} and 600 cm^{-1} with a resolution of 4 cm^{-1} were used for the scan, and each spectrum was collected from an average of 10 measurements.

2.6. Statistical analysis

Differences among the samples were evaluated at 95% confidence level ($p \leq 0.05$) by analysis of variance (ANOVA) following Tukey's test. Open-source R software (https://www.r-project.org) was employed for the analysis.

3. Results

3.1. Mechanical properties of the P(3HB-*co*-3HHx)/HA nanocomposites

The performance of the 3D-printed samples in tensile tests is displayed in Figures 2, and Figure 3 shows the tensile test curves obtained. Tensile specimens printed with different raster angles are compared to those produced by injection molding in a previous work.[58] In any case, regardless of the manufacturing method, composites with the largest proportion of nHA (10%) consistently showed the lowest average values for the ultimate tensile strength and elongation at break. Nonetheless, nHA also increased the stiffness of P(3HB-*co*-3HHx), as the tensile modulus of the composites with 10% of nHA was significantly higher than the rest of combinations for all the production processes. It can be inferred that the reinforcement effect produced by the nanoparticles limits the mobility of the polymer chains during tensile tests.[59]

In the comparison of samples with the same proportion of nHA, differences arise due to the high dependence of the additive manufacturing parameters employed in terms of raster angle. Those with the raster aligned with the tensile effort direction (0°) resulted in the best outputs in tensile strength and stiffness (tensile modulus), since a favorable monoaxial orientation of P(3HB-*co*-3HHx) improves the mechanical behavior.[60] In agreement with this result, other authors have reported that additive manufactured samples of PLA obtained the best tensile strength values for raster angles between 0° and 20°.[61] Under these conditions, stress is transferred along the deposited lines. Bigger raster angles imply transmission of mechanical stress at the interfaces of adjacent deposited lines, so the strength is limited by their adhesion.[62] Nonetheless, for the elongation at break, the 45°/–45° disposition provided the best results. In this case, the lines deposited have certain ability to rotate, allowing for a slightly greater deformation before rupture as described by Santo *et al.*[63] All these effects show the typical anisotropic behavior of an additive manufactured sample.[64]

In injection molding, the packing pressure applied avoids pore generation, so the best mechanical properties are obtained.[65] As an exception to this trend that appeared in this work, samples with a raster angle of 0° improved the tensile strength attained by injection molding for all of P(3HB-*co*-3HHx)/(HA) composites, regardless of the composition. Porosity formation is a well-known limitation of 3D printing by the way that the polymer lines are deposited next to each other.[66] Pore formation limits, in most cases, the mechanical behavior of the 3D-printed samples. Lay *et al.* reported different polymers like PLA, ABS, or nylon; the injection molding samples achieved higher values in terms of tensile strength, tensile modulus and elongation at break than the ones obtained by additive manufacturing.[67] The differences were linked to the presence of voids in the 3D-printed samples.[67] The polymeric matrix employed herein is highly sensitive to the shear rates applied. In the injection molding process, it is necessary to completely fill the mold cavity before polymer

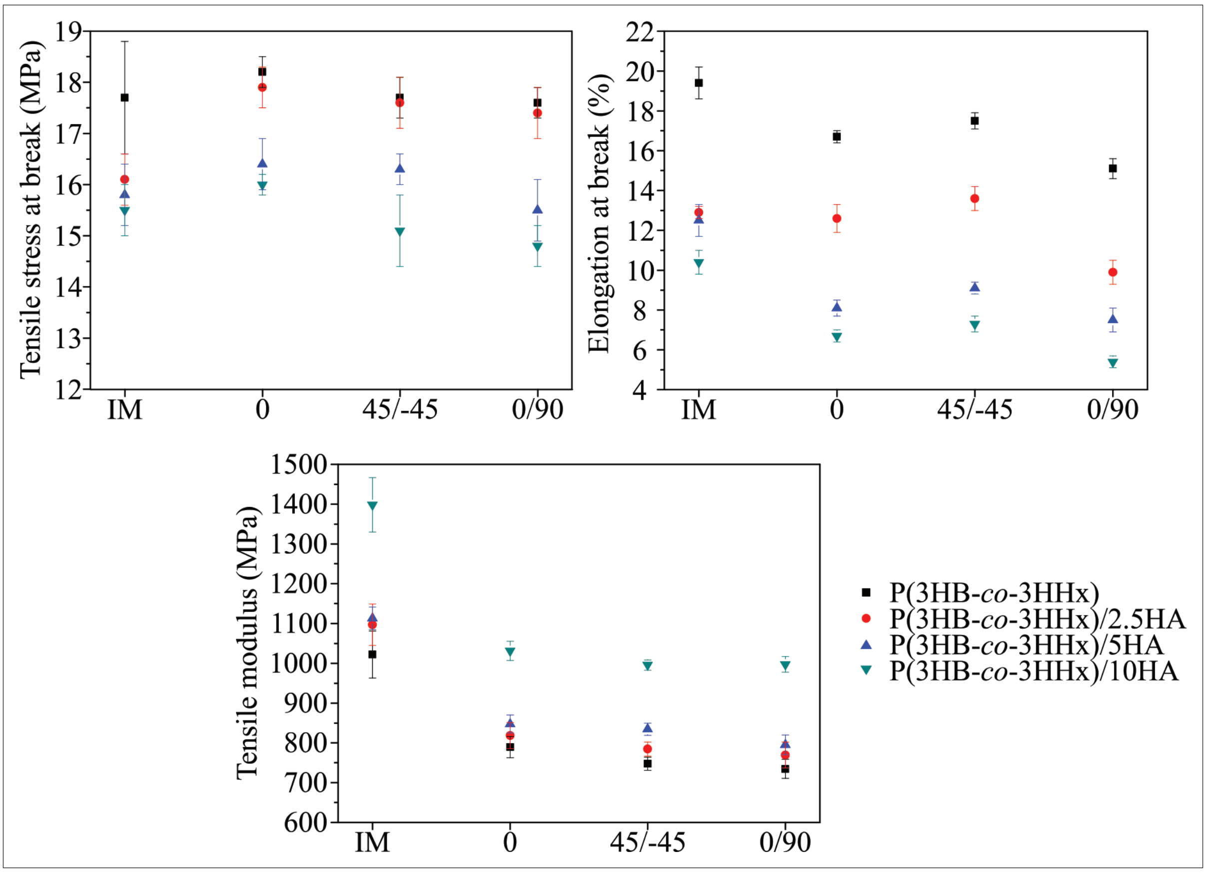

Figure 2. Mechanical properties of the P(3HB-*co*-3HHx)/HA tensile specimens at different raster angles and compared to injection molding (IM).[58]

solidification to prevent high shear stress. The high shear stress promotes chain breakage and reduces molecular weight, leading to a diminishment of key mechanical properties, as observed in PLA during injection molding.[68,69] In contrast, lower shear rates are necessary in an extrusion process like the filament fabrication. Thus, the samples produced by additive manufacturing are subjected to a less aggressive process in terms of shear rate. This is also why, in the absence of nHA, P(3HB-*co*-3HHx)-printed samples maintained greater tensile strength than those obtained by injection. Taking everything into account, the lack of depolymerization during 3D printing might compensate for its detrimental induction of porosity.

3.2 Thermal properties of the P(3HB-*co*-3HHx)/HA nanocomposites

Figure 4 shows the DSC thermograms of P(3HB-*co*-3HHx) and its composites produced after each thermal cycle, *i.e.*, melt blending extrusion process (E), 3D printing filament fabrication (F), and 3D part printing (3D). In addition, the temperatures at which the thermal transitions occurred and their enthalpies are summarized in Table 3. Given that P(3HB-*co*-3HHx) is a copolymer with two kinds of functional ester groups and with alkyl chains, the presence of distinct functional groups promotes the formation of various kind of crystals that melt at different temperatures, resulting in three melting peaks between 108°C and 162°C. This behavior in which three melting peaks appear in P(3HB-*co*-3HHx) was also reported by Farrag *et al.* who proposed that the first melting peak is attributed to secondary lamellae melting, the second one to the primary lamellae melting, and the last one to the reorganization and thickening of lamellae during heating.[70] Around 50°C, an exothermic peak due to a cold crystallization process can be observed. Moreover, the change of baseline at 0°C–5°C is linked with the glass transition temperature. All these temperatures were not qualitatively modified by the introduction of nHA, which however has been reported in the case of nanocomposites of PLA and nHA by other authors.[71]

The different thermal cycles at which the 3D-printed samples were submitted promoted a difference in the characteristic transition temperatures. The biggest differences emerged for the cold crystallization temperature, which was reduced from 52.1°C for P(3HB-*co*-3HHx) after

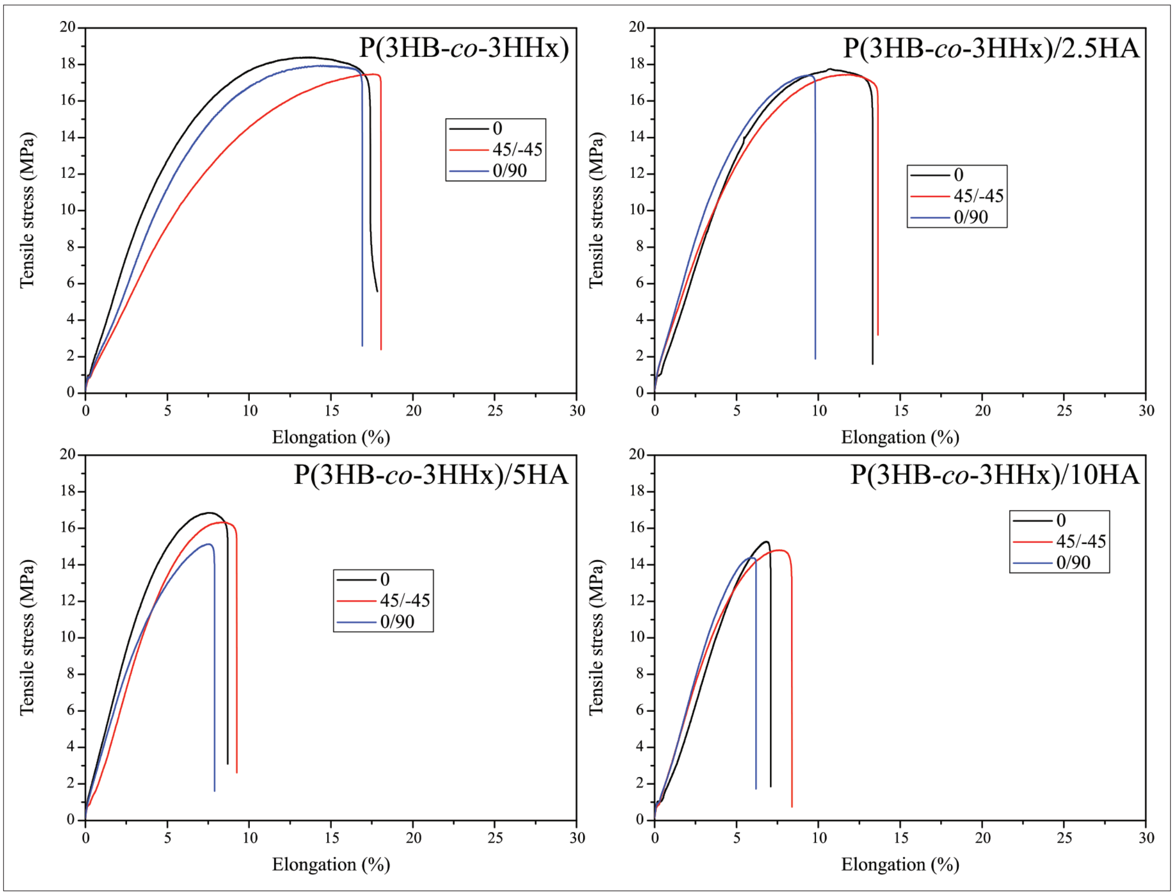

Figure 3. Effect of infill pattern and nHA content on the tensile test curves.

Table 3. DSC characteristics of the P(3HB-*co*-3HHx)/HA nanocomposites

Code		T_g (°C)	T_{cc} (°C)	T_{m1} (°C)	T_{m2} (°C)	T_{m3} (°C)	H_{cc} (J/g)	H_m (J/g)	X_c (%)
P(3HB-*co*-3HHx)	E	0.8 ± 0.2^{a}	52.1 ± 0.1^{a}	108.5 ± 0.1^{a}	125.2 ± 0.1^{a}	161.3 ± 0.2^{a}	27.7 ± 0.2^{a}	49.6 ± 0.2^{a}	15.0 ± 0.2^{a}
	F	1.0 ± 0.1^{b}	50.1 ± 0.2^{a}	109.5 ± 0.3^{a}	126.7 ± 0.2^{a}	161.5 ± 0.2^{a}	27.1 ± 0.3^{a}	49.5 ± 0.3^{a}	15.3 ± 0.1^{a}
	3D	0.8 ± 0.1^{b}	49.6 ± 0.1^{b}	109.9 ± 0.2^{a}	126.5 ± 0.2^{a}	161.4 ± 0.1^{a}	24.0 ± 0.3^{b}	50.9 ± 0.1^{a}	18.5 ± 0.1^{b}
P(3HB-*co*-3HHx)/2.5HA	E	1.1 ± 0.2^{c}	54.3 ± 0.2^{a}	110.6 ± 0.1^{a}	126.9 ± 0.1^{a}	161.6 ± 0.2^{a}	28.0 ± 0.1^{b}	45.0 ± 0.1^{b}	11.9 ± 0.1^{c}
	F	1.0 ± 0.1^{d}	54.3 ± 0.1^{a}	110.9 ± 0.3^{a}	126.9 ± 0.1^{a}	161.6 ± 0.1^{a}	26.7 ± 0.1^{b}	45.5 ± 0.1^{c}	13.2 ± 0.1^{d}
	3D	1.0 ± 0.1^{e}	54.1 ± 0.2^{a}	111.0 ± 0.3^{a}	127.1 ± 0.1^{a}	161.8 ± 0.1^{a}	23.5 ± 0.1^{c}	45.1 ± 0.1^{d}	15.2 ± 0.1^{d}
P(3HB-*co*-3HH x)/5HA	E	1.0 ± 0.1^{f}	54.3 ± 0.2^{a}	111.2 ± 0.3^{a}	126.6 ± 0.1^{a}	161.9 ± 0.2^{a}	27.2 ± 0.1^{c}	37.3 ± 0.1^{e}	7.3 ± 0.1^{e}
	F	0.8 ± 0.1^{f}	55.5 ± 0.1^{c}	110.9 ± 0.2^{a}	126.8 ± 0.2^{a}	161.3 ± 0.2^{a}	25.1 ± 0.1^{d}	37.3 ± 0.1^{f}	8.8 ± 0.1^{f}
	3D	0.8 ± 0.1^{f}	55.6 ± 0.1^{d}	111.0 ± 0.1^{a}	128.6 ± 0.1^{a}	161.5 ± 0.1^{a}	24.4 ± 0.1^{e}	37.7 ± 0.1^{g}	9.6 ± 0.1^{g}
P(3HB-*co*-3HH x)/10HA	E	0.7 ± 0.1^{g}	57.1 ± 0.2^{e}	112.1 ± 0.2^{a}	128.4 ± 0.2^{a}	161.8 ± 0.1^{a}	29.7 ± 0.1^{f}	36.2 ± 0.1^{h}	4.9 ± 0.1^{h}
	F	0.6 ± 0.2^{h}	58.1 ± 0.1^{f}	111.6 ± 0.2^{a}	128.7 ± 0.1^{a}	161.2 ± 0.2^{a}	26.7 ± 0.1^{f}	36.3 ± 0.1^{i}	7.3 ± 0.1^{i}
	3D	0.8 ± 0.1^{h}	57.9 ± 0.1^{g}	111.7 ± 0.1^{a}	127.7 ± 0.2^{a}	161.3 ± 0.1^{a}	25.0 ± 0.1^{g}	36.9 ± 0.1^{j}	9.0 ± 0.1^{j}

Notes: $^{a–j}$ Different letters in the same column indicate a significant difference among the samples ($p < 0.05$). E Extrusion; F, Filament; 3D, 3D print.

the first extrusion process to 49.6°C after 3D printing. Similar results were reported after a recycling process on dried and wet PLA.[72] This phenomenon was caused by the reduction in molecular weight of the polymer chains that occurred due to the successive thermal cycles at which the sample was submitted. This effect was also reported by Chaitanya *et al*. after performing a recycling process of PLA.[73] The presence of nHA reduced these differences,

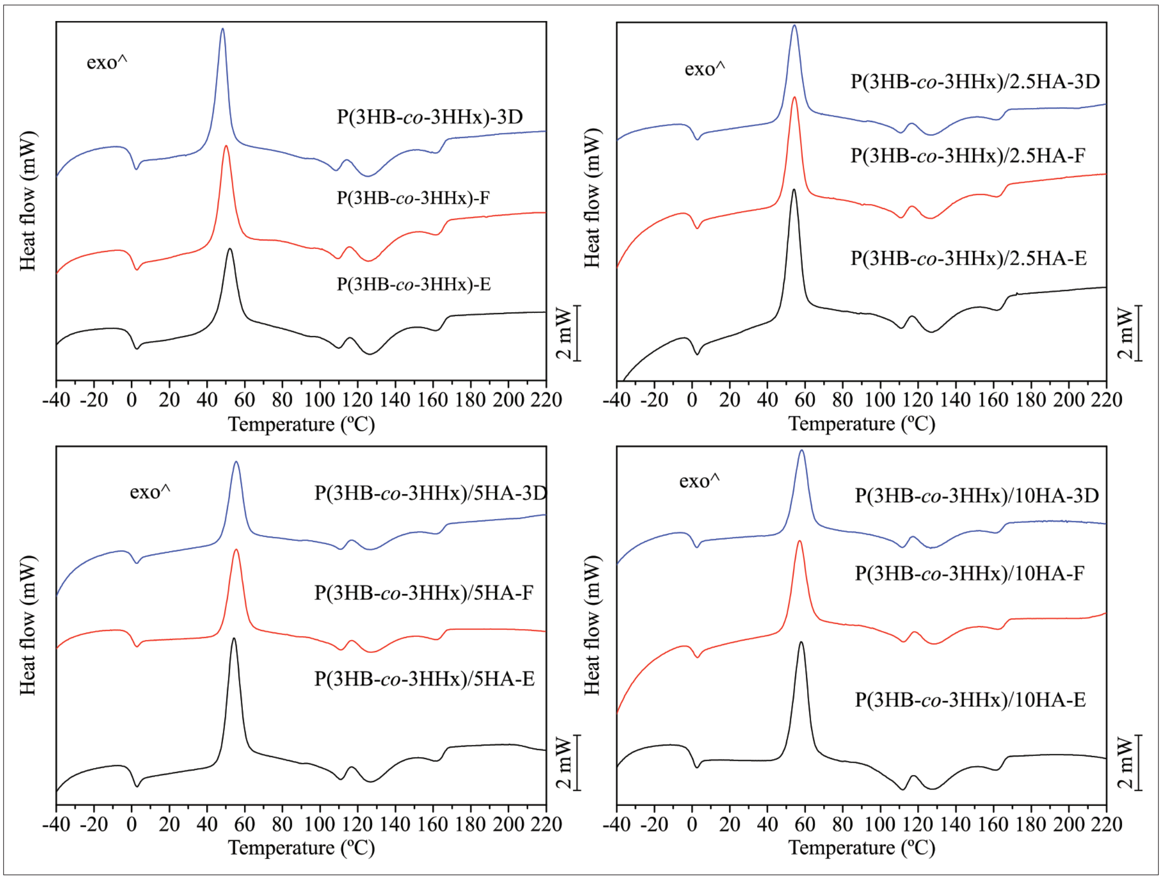

Figure 4. DSC thermograms of the second heating cycle of the P(3HB-*co*-3HHx)/HA nanocomposites.

similar to the effects found for the incorporation of cloisite into a polypropylene matrix.[74]

Regarding melting enthalpies, the differences between the thermal cycles were almost insignificant, whereas the cold crystallization enthalpy decreased notably. During each cycle, polymer chains were cleaved to a certain extent. This prompted the rearrangement of the polymer chains during the cooling cycle, and thus, the degree of crystallinity increased. This behavior is a typical effect when reprocessing polymers.[75]

Generally, the addition of nHA did not affect the main characteristic temperatures but had a significant influence on the degree of crystallinity. The introduction of the nanoparticles implied the establishment of new filler–matrix interactions, partially replacing previous polymer–polymer interactions that hindered the recrystallization.[76]

The thermal degradation behavior is shown in Figure 5. Table 4 shows the key temperature values from the TGA and derivative thermogravimetric analysis (DTG) (first derivative) curves: the initial degradation temperature ($T_{5\%}$), regarded as the temperature at which the sample had lost the 5% of its initial mass; the temperature of maximum degradation rate (T_{max}), and the weight of the remaining sample at 700°C (residual weight). For all the different samples analyzed, $T_{5\%}$ values were ranged between 261°C and 271°C. Small amounts of nHA (2.5 wt%) increased the initial degradation temperature, but higher amounts of nanoparticles reduced the thermal stability of the sample. The improvement of the thermal stability with the addition of hydroxyapatite is also reported by Trakoolwannachai *et al.*[77] Despite this, the cleavage of polymer chains due to the thermal cycles promoted a slight reduction in the thermal stability of the samples analyzed.[78] Such reduction is not relevant enough to limit the manufacturing process.[79]

Regarding T_{max}, a significant improvement was obtained when nHA up to 5 wt% was added, with values around 292°C. However, increasing the proportion of nHA to 10% provoked a decrease, likely related to the trend followed by the crystallinity measured by DSC. All in all, the ceramic structure of these nanoparticles provides a high thermal stability, since nHA does not degrade below 700°C. This improvement was caused by the formation of strong hydrogen bonds between the polymer (the acceptor) and the nanofiller (the donor).[80]

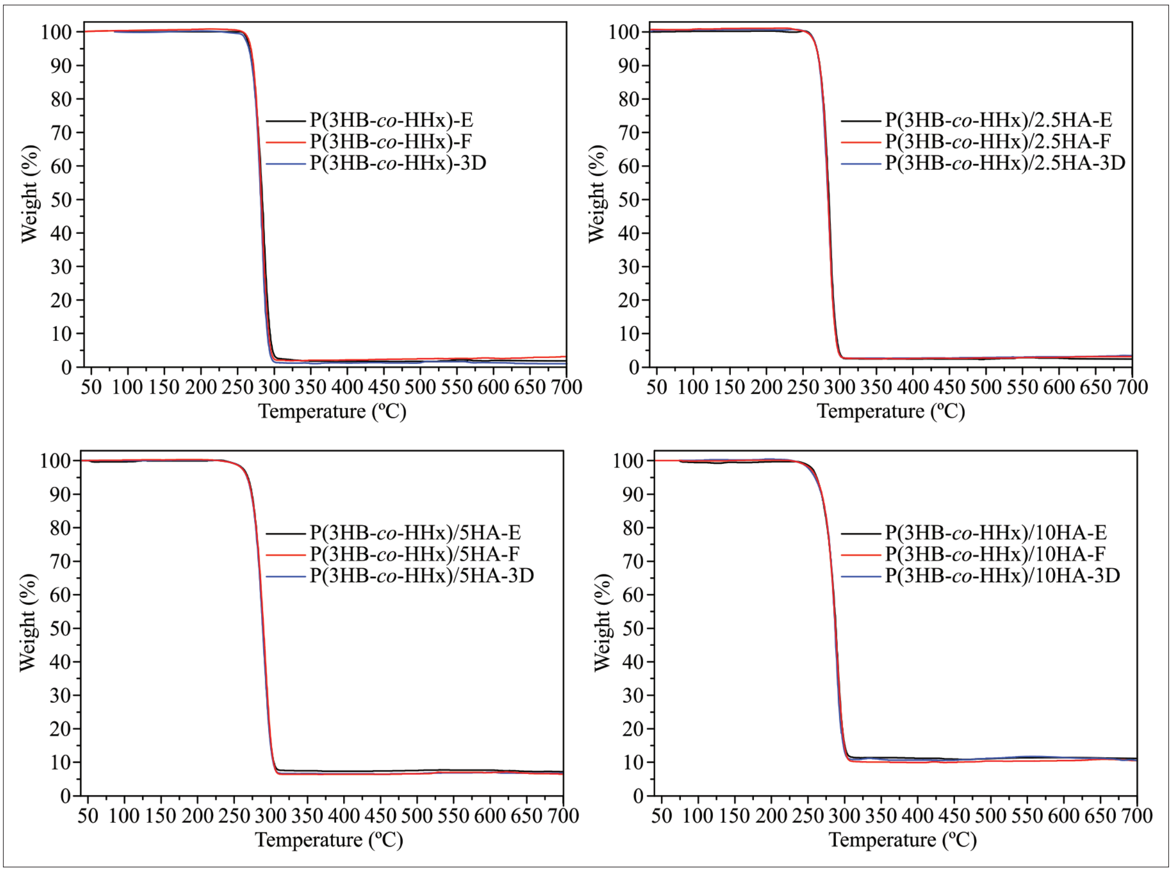

Figure 5. TGA curves of the P(3HB-*co*-3HHx)/HA nanocomposites.

Table 4. Thermal degradation properties of the P(3HB-*co*-3HHx)/HA nanocomposites

Code		$T_{5\%}$ (°C)	T_{max} (°C)	Residual weight (%)
P(3HB-*co*-3HHx)	E	267.5 ± 0.5[a]	283.4 ± 0.3[a]	2.1 ± 0.2[a]
	F	270.3 ± 0.6[a]	281.2 ± 0.4[a]	3.2 ± 0.3[b]
	3D	266.1 ± 0.7[a]	280.3 ± 0.2[a]	1.8 ± 0.3[c]
P(3HB-*co*-3HHx)/2.5HA	E	271.2 ± 0.4[a]	288.2 ± 0.2[a]	2.5 ± 0.4[d]
	F	269.8 ± 0.5[a]	286.7 ± 0.4[a]	2.7 ± 0.3[e]
	3D	269.9 ± 0.5[a]	285.8 ± 0.5[a]	3.4 ± 0.2[f]
P(3HB-*co*-3HHx)/5HA	E	268.7 ± 0.4[a]	293.5 ± 0.3[a]	7.1 ± 0.5[g]
	F	267.9 ± 0.4[a]	292.0 ± 0.2[a]	6.8 ± 0.4[h]
	3D	267.1 ± 0.3[a]	291.1 ± 0.5[a]	6.6 ± 0.3[i]
P(3HB-*co*-3HHx)/10HA	E	262.5 ± 0.5[a]	288.7 ± 0.5[a]	12.4 ± 0.4[j]
	F	261.6 ± 0.4[a]	286.8 ± 0.4[a]	11.9 ± 0.3[k]
	3D	261.1 ± 0.3[a]	285.4 ± 0.4[a]	11.9 ± 0.4[l]

Notes: [a–l] Different letters in the same column indicate a significant difference among the samples ($p < 0.05$). E, Extrusion; F, Filament; 3D, 3D Print.

Finally, owing to the non-degradation of nHA between 50°C and 700°C, the residue obtained at the end of the test is proportional to its fraction in each material.

3.3 Rheological properties of the P(3HB-*co*-3HHx)/HA nanocomposites

The rheological properties (Figure 6) of the different composites showed shear-thinning of a non-Newtonian behavior or pseudoplastic behavior that promotes a reduction in viscosity with the shear rate.[81] First, a

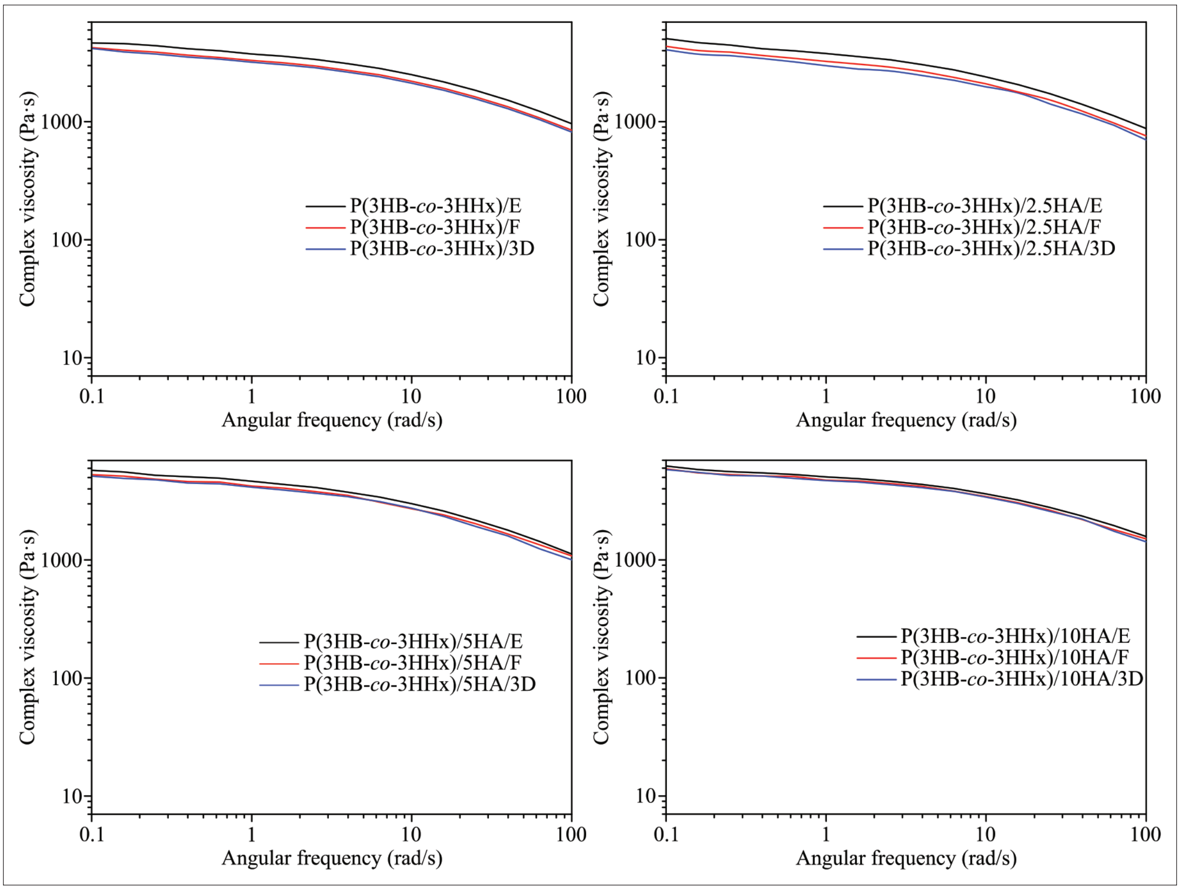

Figure 6. Rheological behavior of the P(3HB-*co*-3HHx)/HA nanocomposites.

reduction in the complex viscosity was observed in each thermal cycle of the sample. For example, in P(3HB-*co*-3HHx) following melt bending extrusion (E), a complex viscosity of 3761 Pa·s at 1 rad/s was obtained, whereas after the 3D printing process, this parameter adopted a value of 3197 Pa·s. This phenomenon also occurs in PLA,[82] thereby confirming the hypothesis of thermal degradation that promotes the chain scission of the polymer chains in each thermal cycle.

When the amount of hydroxyapatite increased, smaller differences between each cycle were recorded. More particle dispersion typically results in higher values of complex viscosity, due to the greater number of particle-matrix interactions.[83] At the same time, during the melting state of the polymer, thermal degradation takes place. Both effects are overlapped during the melt processing of the materials. As a result, after each thermal cycle, complex viscosity decreased, but the differences that arose became smaller.

Additionally, depending on the amount of nHA considered, an increase in complex viscosity was obtained due to the increase of the nanofiller. This is a typical behavior after the incorporation of particles in a polymer.[84]

Table 5. Scaffold porosity results

Code	Material density (g/cm^3)	Scaffold porosity
P(3HB-co-3HHx)	1.215 ± 0.008[a]	0.378 ± 0.004[a]
P(3HB-co-3HHx)/2.5HA	1.254 ± 0.007[a]	0.376 ± 0.005[a]
P(3HB-co-3HHx)/5HA	1.263 ± 0.007[a]	0.373 ± 0.003[a]
P(3HB-co-3HHx)/10HA	1.352 ± 0.010[b]	0.371 ± 0.005[a]

Notes: [a,b] Different letters in the same column indicate a significant difference among the samples ($p < 0.05$).

3.4. Scaffolds porosity of the P(3HB-*co*-3HHx/HA) nanocomposites

Table 5 shows the scaffold porosity and standard deviation obtained for each material composition. It is worth noticing that the introduction of hydroxyapatite increased the density of the composites due to the presence of the ceramic material.[25] The values obtained for the density ranged from 1.215 g/cm^3 for the neat polymer up to 1.352 g/cm^3 for the composite with the highest ceramic content.

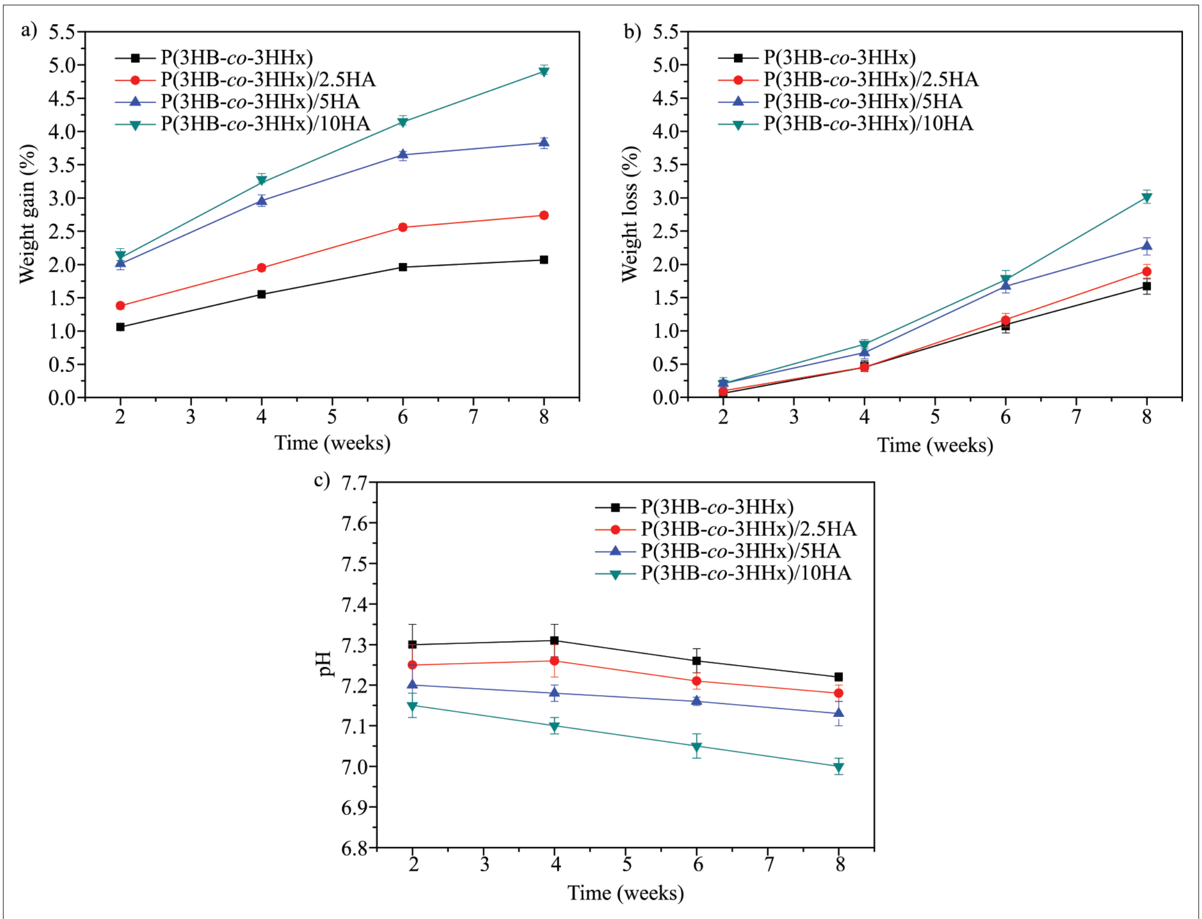

Figure 7. Effect of the immersion in PBS on (a) weight gain, (b) weight loss, and (c) pH changes of the P(3HB-*co*-3HHx)/HA nanocomposites over time.

Regarding the porosity obtained, with the manufacturing conditions (70% infill), the calculated values were in all cases close to 0.4, with a difference of 1.9% between all the compositions prepared. The porosity values obtained are higher than the values expected by the amount of infill programmed during the slicing process. In this sense, Vaezi *et al*. proposed that this difference emerges due to the manufacturing process itself, which generates porosity even when scaffolds are manufactured with an infill density of 100%.[85]

3.5. Saline degradation in PBS of the P(3HB-*co*-3HHx)/HA nanocomposites

The immersion of the scaffolds in PBS for 8 weeks generated different effects, as indicated in Figure 7. The first of them was the modification of the weight of the sample as a function of the time elapsed (Figure 7a). The scaffold mass increased until a weight gain of 4.9% for the P(3HB-*co*-3HHx)/10HA composite or 2.1% for the P(3HB-*co*-HHx) was reached. Similarly, the introduction of hydroxyapatite into a polymeric matrix increased the hydrophilicity of the material, promoting a higher moisture sorption during the assay.[86] After drying, the weight of the scaffolds was reduced to 3.0% for the composite with 10 wt% nHA at the end of week 8 by a degradation process occurred during the immersion. In this sense, some authors have reported that polymers such as PLA were not significantly degraded at 37°C during 8 weeks of immersion.[87] Other works reported weight losses up to 6% for polycaprolactone at room temperature.[30] The degradation of the scaffold (Figure 7b) starts with a cleavage of polymer chains at neutral or close-to-neutral pH medium by nucleophilic additions of water on carbonyl groups. In addition, the dissolution and the capillary water uptake of nHA particles boosted the degradation rate, as proposed by Sultana *et al*.[88] Additionally, it is noteworthy that, even with the highest proportion of nHA, the diffusion rate of ions through the material was not high enough to prompt harsh pH variation. This is beneficial to the potential biocompatibility of the scaffold, as it helps avoid catalyzing adverse reactions in contact with the human body. Kim *et al*. also reported a pH reduction during a degradation process of a PLGA

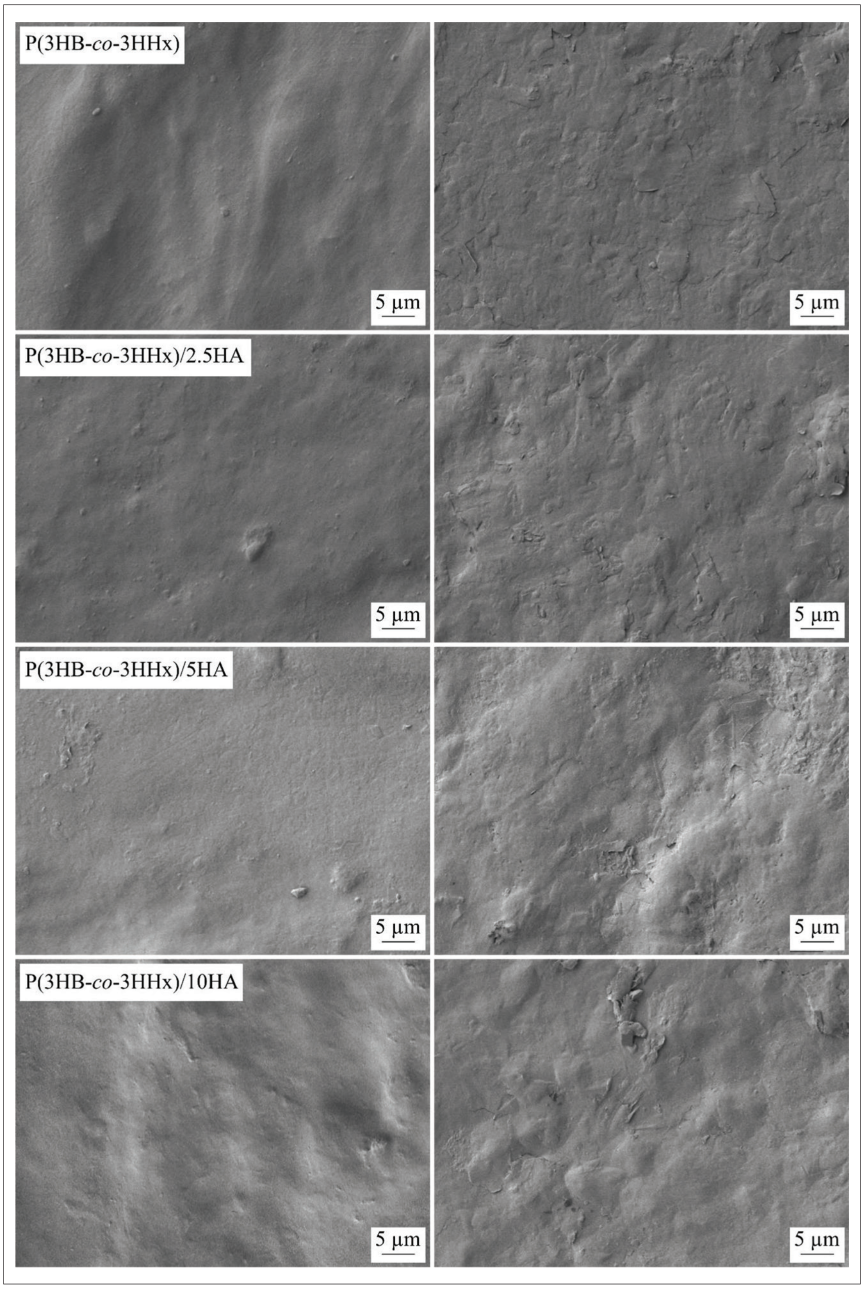

Figure 8. FE-SEM images of the surface of the P(3HB-co-3HHx)/HA nanocomposites with different compositions at week 0 (left) and week 8 (right). Images taken at a magnification of 1000×.

due to the realized degradation products that appear in the solution.[89]

Figure 8 indicates the changes of the surface during these eight weeks and, especially in the cases of high nHA proportion (5% and 10%), mineralization by Ca-P deposition occurs. It should be noted that this deposition of phosphorus-containing salts onto the surface of the scaffold could help to increase the biocompatibility, since it eases osteoblast attachment and cell adhesion.[90] This change in terms of biocompatibility should be properly assessed by cellular test in order to measure the changes in cell proliferation.

From the point of view of mechanical behavior, scaffolds suffered a loss of compression strength that was proportional to the immersion time, as can be observed in Figure 9. Hydrolytic degradation during immersion led to a reduction in the molecular weight of the polymer.[90] For example, the P(3HB-*co*-3HHx)/10HA composite, prior to immersion,

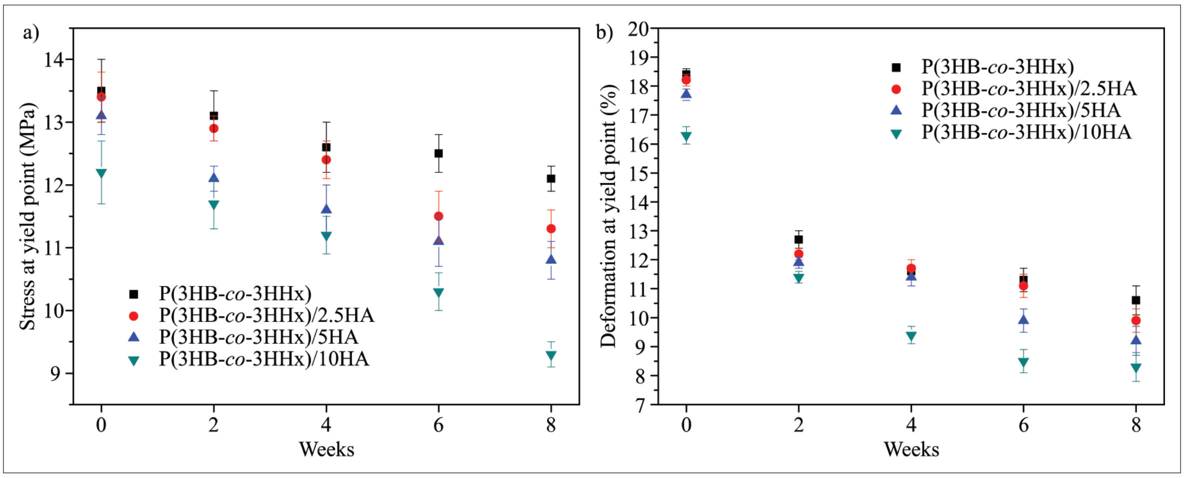

Figure 9. Compression properties of the scaffolds at different immersion times in terms of (a) stress at yield point and (b) deformation at yield point.

showed a compressive stress at yield point of 12.2 MPa with a deformation at break of 16.3%. After 8 weeks of immersion, compressive stress at yield point of 9.3 MPa and deformation at break of 8.3% were measured, respectively.

As in tensile tests on 3D-printed specimens, the best strength and deformation values were obtained for the polymeric material without hydroxyapatite. The incorporation of an increasing amount of the osteoconductive additive promoted a reduction of mechanical properties such as the stress and deformation at yield point, as shown in Figure 10. Similar effects under compression tests have been reported for additive manufactured scaffolds made of PLA and nHA.[91]

3.6. Chemical analysis of the PBS of the P(3HB-*co*-3HHx)/HA nanocomposites

Figure 11 shows the chemical analysis of the surface of the scaffolds before and after immersion in PBS. The scaffolds before immersion showed characteristic peaks of P(3HB-*co*-3HHx) at 1719 cm^{-1} belonging to the C=O stretching vibration of the crystalline region of the polymeric structure. Additionally, peaks also appeared at 2928 cm^{-1} and 2850 cm^{-1} corresponding to C-H vibration and asymmetric stretching of CH_2, respectively.[32,92] For the composites with hydroxyapatite, a peak appeared in the range between 1020 cm^{-1} and 1080 cm^{-1}, which corresponds to the phosphate groups present in HA.[93] The presence of this peak was more noticeable when the amount of hydroxyapatite in each composite was increased. After immersion, the spectrum of the scaffolds changed significantly because a coating layer was formed on the polymer surface, resulting in the disappearance or the low intensity of peaks that could be observed at 2928 cm^{-1} and 2850 cm^{-1} and the reduction of intensity at 1719 cm^{-1} (Figure 11b). The peak associated to hydroxyapatite (1020–1080 cm^{-1}) appeared in all the composites considered because during the immersion in PBS, a hydroxyapatite layer was formed, as observed in the morphology of the surface analysis.[94]

4. Conclusion

This work showed that P(3HB-*co*-3HHx)/HA composites can be effectively used for the fabrication of scaffolds by FDM. The manufacturing method involved different thermal treatments, including a compounding process to obtain the composites, an extrusion process to obtain the filaments employed in the FDM process, and a 3D printing process to obtain the samples. All these cycles resulted in slight thermal degradation, as seen from DSC studies with a higher degree of crystallinity and a lower cold crystallization temperature. DSC test also indicated that the incorporation of ceramic nanoparticles decreased the crystallinity of the material. TGA showed that cleavage of polymer chains reduced the T_{max} up to 3°C for the same composite. The degradation effect was also observed in the rheology analysis, as each of the thermal cycles promoted a slight reduction of viscosity as a result of the incorporation of nHA.

Overall, increasing the amount of nHA in the composites decreased their tensile strength and their ductility. On the other hand, their stiffness increased with a tensile modulus near 750 MPa for the neat polymer, while values near 950 MPa for the 10 wt% nHA were obtained. Regarding the pattern employed, the raster angle of 0°gave rise to the highest strength, while the best ductility was obtained with the 45°/–45° pattern with a 17.5% value in the elongation at break. The compression behavior of the scaffolds was diminished in the case of high amounts of nHA, presenting 13.5 MPa for the neat polymer at week 0 and 12.2 MPa for the 10 wt% nHA. Moreover, samples were subjected to an immersion process in PBS solution

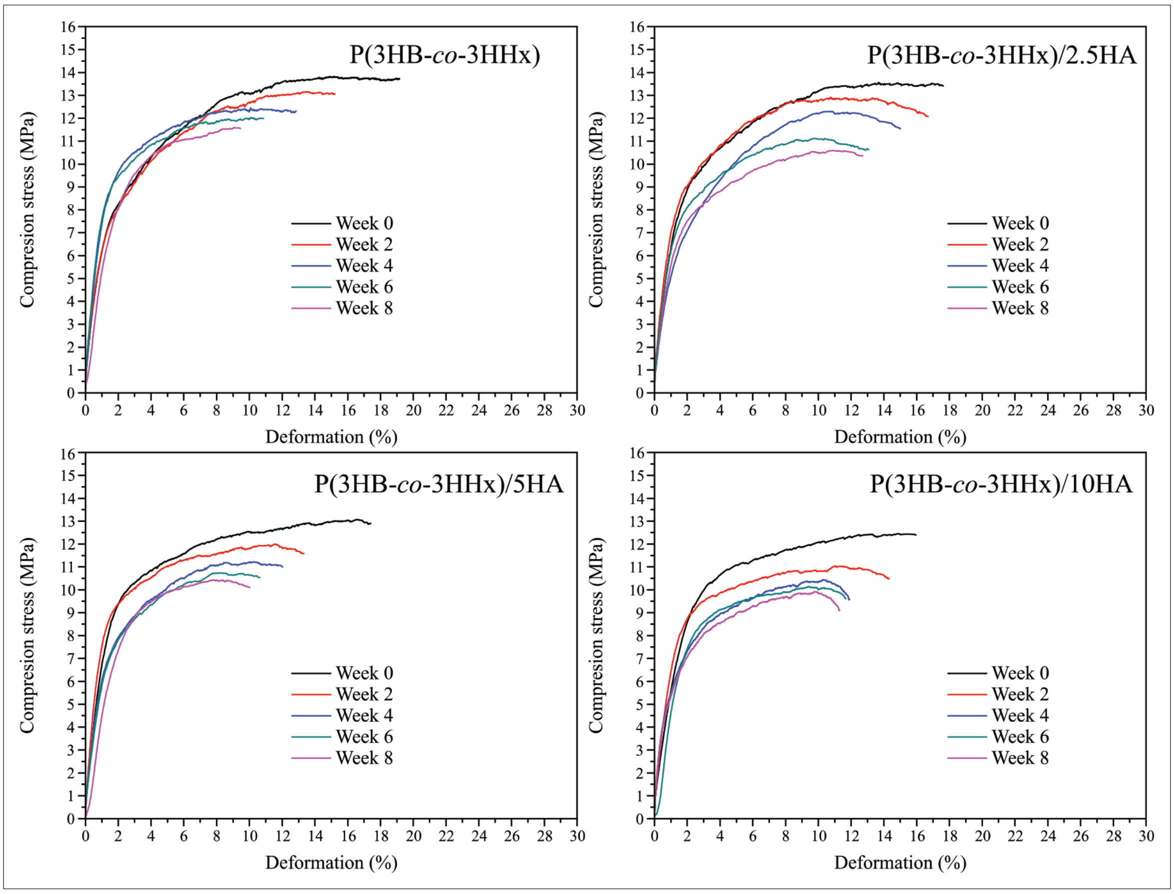

Figure 10. Effect of the nanohydroxyapatite and the immersion time in terms of compression properties.

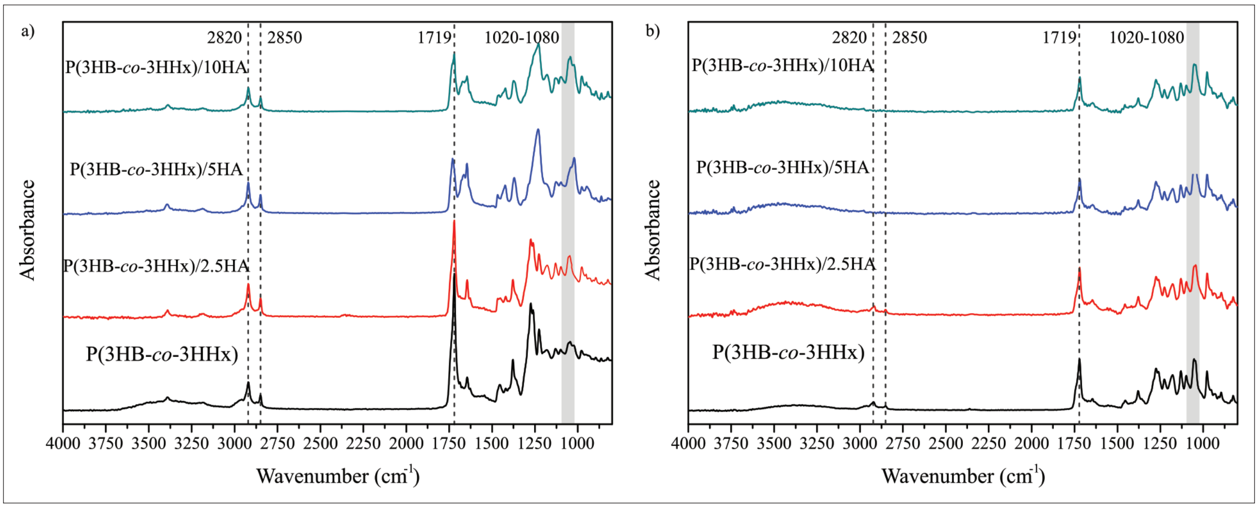

Figure 11. Surface chemical composition measured by ATR-FTIR of the scaffolds: (a) week 0 and (b) week 8.

for 8 weeks, which resulted in certain degradation as observed from mass reduction up to 3.0% and loss of mechanical properties up to 9.3 MPa for the 10 wt% nHA at week 8. The immersion process led to only slight changes in the pH of the medium and to hydroxyapatite deposition on the scaffold surface, as observed in the FTIR analysis and the surface morphology, which could help with the biocompatibility. Regarding this key aspect, *in vivo* studies should be included in future studies.

Acknowledgments

Juan Ivorra-Martinez wants to thank for the FPU19/01759 grant funded by MCIN/AEI/10.13039/501100011033 and, as appropriate, by ESF Investing in Your Future. Funding for open-access charge is provided by Universitat Politècnica de València (UPV). Marc Delgado-Aguilar is a Serra Húnter Fellow. Microscopy Services at UPV are also acknowledged for their help in collecting and analyzing images.

Funding

This work is supported by the grant PID2020-116496RB-C22 funded by MCIN/AEI/10.13039/501100011033 and the grant TED2021-131762A-I00 funded by MCIN/AEI/10.13039/501100011033 and by the European Union. Authors also thank Generalitat Valenciana-GVA for funding this research through the grant numbers AICO/2021/025 and CIGE/2021/094. This study is also funded by Aid for First Research Projects (PAID-06-22), Vice-rectorate for Research of the Universitat Politècnica de València (UPV).

Conflict of interest

The authors declare no conflicts of interest.

Author contributions

Conceptualization: Ines Ferrer, Maria Luisa Garcia-Romeu
Formal analysis: Juan Ivorra-Martinez
Fund acquisition: Marc Delgado-Aguilar, Roberto Aguado
Project administration: Ines Ferrer, Maria Luisa Garcia-Romeu
Visualization: Juan Ivorra-Martinez
Writing – original draft: Juan Ivorra-Martinez
Writing – review & editing: Juan Ivorra-Martinez, Marc Delgado-Aguilar, Teodomiro Boronat

Ethics approval and consent to participate

None.

Consent for publication

None.

Availability of data

Data will be made available on request.

References

1. Ngo TD, Kashani A, Imbalzano G, Nguyen KTQ, Hui D. Additive manufacturing (3D printing): A review of materials, methods, applications and challenges. *Compos B Eng*. 2018;143(1): 172-196. doi: 10.1016/j.compositesb.2018.02.012
2. Mohan N, Senthil P, Vinodh S, Jayanth N. A review on composite materials and process parameters optimisation for the fused deposition modelling process. *Virtual Phys Prototyp*. 2017;12(1):47-59. doi: 10.1080/17452759.2016.1274490
3. Martín-Montal J, Pernas-Sánchez J, Varas D. Experimental characterization framework for SLA additive manufacturing materials. *Polymers*. 2021;13(7):1-16. doi: 10.3390/polym13071147
4. Lima AL, Pires FQ, Hilgert LA, Sá-Barreto LL. Oscillatory shear rheology as an in-process control tool for 3D printing medicines production by fused deposition modeling. *J Manuf Process*. 2022;76(1):850-862. doi: 10.1016/j.jmapro.2022.03.001
5. Tarrés Q, Melbø JK, Delgado-Aguilar M, Espinach FX, Mutjé P, Chinga-Carrasco G. Bio-polyethylene reinforced with thermomechanical pulp fibers: Mechanical and micromechanical characterization and its application in 3D-printing by fused deposition modelling. *Compos B Eng*. 2018;153(1):70-77. doi: 10.1016/j.compositesb.2018.07.009
6. Domínguez-Robles J, Utomo E, Cornelius VA, et al. TPU-based antiplatelet cardiovascular prostheses prepared using fused deposition modelling. *Mater Design*. 2022;220(1):1-18. doi: 10.1016/j.matdes.2022.110837
7. Prasad LK, Smyth H. 3D printing technologies for drug delivery: A review. *Drug Dev Ind Pharm*. 2016;42(7):1019-1031. doi: 10.3109/03639045.2015.1120743
8. Roopavath UK, Kalaskar DM. Introduction to 3D printing in medicine, In: *3D Printing in Medicine*. 2017;Elsevier Inc., 1-20.
9. Yan Q, Dong H, Su J, et al. A review of 3D printing technology for medical applications. *Engineering*. 2018;4(5): 729-742. doi: 10.1016/j.eng.2018.07.021
10. Stansbury JW, Idacavage MJ. 3D printing with polymers: Challenges among expanding options and opportunities. *Dent Mater*. 2016;32(1):54-64. doi: 10.1016/j.dental.2015.09.018
11. Chen X, Gao C, Jiang J, Wu Y, Zhu P, Chen G. 3D printed porous PLA/nHA composite scaffolds with enhanced osteogenesis and osteoconductivity in vivo for bone regeneration. *Biomed Mater (Bristol)*. 2019;14(6):1-15. doi: 10.1088/1748-605X/ab388d
12. Dwivedi R, Kumar S, Pandey R, et al. Polycaprolactone as biomaterial for bone scaffolds: Review of literature. *J Oral Biol Craniofac Res*. 2020;10(1):381-388. doi: 10.1016/j.jobcr.2019.10.003
13. Dhandayuthapani B, Yoshida Y, Maekawa T, D. Kumar S. Polymeric scaffolds in tissue engineering application: A review. *Int J Polym Sci*. 2011;2011(1):1-19. doi: 10.1155/2011/290602

14. Billström GH, Blom AW, Larsson S, Beswick AD. Application of scaffolds for bone regeneration strategies: Current trends and future directions. *Injury*. 2013;44(suppl.1):S28-S33. doi: 10.1016/S0020-1383(13)70007-X

15. Betz MW, Yeatts AB, Richbourg WJ, et al. Macroporous hydrogels upregulate osteogenic signal expression and promote bone regeneration. *Biomacromolecules*. 2010;11(5):1160-1168. doi: 10.1021/bm100061z

16. Webster TJ, Ahn ES. Nanostructured biomaterials for tissue engineering bone. *Adv Biochem Eng/Biotechnol*. 2006;103(1):275-308. doi: 10.1007/10_021

17. Javaid M, Haleem A. 3D printing applications towards the required challenge of stem cells printing. *Clin Epidemiol Global Health*. 2020;8(3):862-867. doi: 10.1016/j.cegh.2020.02.014

18. Strong D, Sirichakwal I, Manogharan GP, Wakefield T. Current state and potential of additive: Hybrid manufacturing for metal parts. *Rapid Prototyp J*. 2017;23(3):577-588. doi: 10.1108/RPJ-04-2016-0065

19. Spierings AB, Starr TL, Wegener K. Fatigue performance of additive manufactured metallic parts. *Rapid Prototyp J*. 2013;19(2):88-94. doi: 10.1108/13552541311302932

20. Song J, Gao H, Zhu G, Cao X, Shi X, Wang Y. The preparation and characterization of polycaprolactone/graphene oxide biocomposite nanofiber scaffolds and their application for directing cell behaviors. *Carbon*. 2015;95(1):1039-1050. doi: 10.1016/j.carbon.2015.09.011

21. Nazeer MA, Onder OC, Sevgili I, Yilgor E, Kavakli IH, Yilgor Iskender. 3D printed poly(lactic acid) scaffolds modified with chitosan and hydroxyapatite for bone repair applications. *Mater Today Commun*. 2020;25(1):1-9. doi: 10.1016/j.mtcomm.2020.101515

22. Kattimani VS, Kondaka S, Lingamaneni KP. Hydroxyapatite: Past, present, and future in bone regeneration. *Bone Tissue Regen Insights*. 2016;7(1):BTRI.S36138. doi: 10.4137/btri.S36138

23. Kim CG, Han KS, Lee S, Kim MC, Kim SY, Nah J. Fabrication of biocompatible polycaprolactone–hydroxyapatite composite filaments for the FDM 3D printing of bone scaffolds. *Appl Sci (Switzerland)*. 2021;11(14):1-9. doi: 10.3390/app11146351

24. Fierz FC, Beckmann F, Huser M, et al. The morphology of anisotropic 3D-printed hydroxyapatite scaffolds. *Biomaterials*. 2008;29(28):3799-3806. doi: 10.1016/j.biomaterials.2008.06.012

25. Esposito Corcione C, Gervaso F, Scalera F, et al. Highly loaded hydroxyapatite microsphere/PLA porous scaffolds obtained by fused deposition modelling. *Ceram Int*. 2019;45(2, Part B):2803-2810. doi: https://doi.org/10.1016/j.ceramint.2018.07.297

26. Yang TC. Effect of extrusion temperature on the physico-mechanical properties of unidirectional wood fiber-reinforced polylactic acid composite (WFRPC) components using fused depositionmodeling. *Polymers*. 2018;10(9):1-11. doi: 10.3390/polym10090976

27. Ang SL, Sivashankari R, Shaharuddin B, et al. Potential applications of polyhydroxyalkanoates as a biomaterial for the aging population. *Polym Degrad Stab*. 2020;181(1):1-18. doi: 10.1016/j.polymdegradstab.2020.109371

28. Asghari F, Samiei M, Adibkia K, Akbarzadeh A, Davaran S. Biodegradable and biocompatible polymers for tissue engineering application: A review. *Artif Cells Nanomed Biotechnol*. 2017;45(2):185-192. doi: 10.3109/21691401.2016.1146731

29. Mehrpouya M, Vahabi H, Barletta M, et al. Additive manufacturing of polyhydroxyalkanoates (PHAs) biopolymers: Materials, printing techniques, and applications. *Mater Sci Eng C*. 2021;127(1):1-13. doi: 10.1016/j.msec.2021.112216

30. Ferrer I, Manresa A, Méndez JA, Delgado-Aguilar M, Garcia-Romeu ML. Manufacturing PLA/PCL blends by ultrasonic molding technology. *Polymers*. 2021;13(15):1-17. doi: 10.3390/polym13152412

31. Wu CS. Characterization, functionality and application of siliceous sponge spicules additive-based manufacturing biopolymer composites. *Addit Manuf*. 2018;22(1):13-20. doi: 10.1016/j.addma.2018.04.034

32. Rebia RA, Rozet S, Tamada Y, Tanaka T. Biodegradable PHBH/PVA blend nanofibers: Fabrication, characterization, in vitro degradation, and in vitro biocompatibility. *Polym Degrad Stab*. 2018;154(1):124-136. doi: 10.1016/j.polymdegradstab.2018.05.018

33. Washington MA, Balmert SC, Fedorchak MV, Little SR, Watkins SC, Meyer TY. Monomer sequence in PLGA microparticles: Effects on acidic microclimates and in vivo inflammatory response. *Acta Biomater*. 2018;65(1):259-271. doi: 10.1016/j.actbio.2017.10.043

34. Lim J, You M, Li J, Li Z. Emerging bone tissue engineering via polyhydroxyalkanoate (PHA)-based scaffolds. *Mater Sci Eng C*. 2017;79(1):917-929. doi: 10.1016/j.msec.2017.05.132

35. dos Santos AJ, Oliveira Dalla Valentina LV, Hidalgo Schulz AA, Tomaz MA. From obtaining to degradation of PHB: Material properties. Part I. *Ingeniería y ciencia*. 2017;13(26):269-298.

36. Ramot Y, Haim-Zada M, Domb AJ, Nyska A. Biocompatibility and safety of PLA and its copolymers. *Adv Drug Deliv Rev*. 2016;107(1):153-162. doi: 10.1016/j.addr.2016.03.012

37. Qu XH, Wu Q, Zhang KY, Chen GQ. In vivo studies of poly(3-hydroxybutyrate-co-3-hydroxyhexanoate) based polymers: Biodegradation and tissue reactions. *Biomaterials*. 2006;27(19):3540-3548. doi: 10.1016/j.biomaterials.2006.02.015

38. Arza CR, Jannasch P, Johansson P, Per Magnusson, Werker A, Maurer FHJ. Effect of additives on the melt rheology and thermal degradation of poly[(R)-3-hydroxybutyric acid]. *J Appl Polym Sci*. 2015;132(15):1-6. doi: 10.1002/app.41836

39. Kovalcik A, Sangroniz L, Kalina M, et al. Properties of scaffolds prepared by fused deposition modeling of poly(hydroxyalkanoates). *Int J Biol Macromol*. 2020;161(1):364-376. doi: 10.1016/j.ijbiomac.2020.06.022

40. Festas AJ, Ramos A, Davim JP. Medical devices biomaterials: A review. *Proc Inst Mech Eng L J Mater Design Appl*. 2020;234(1):218-228. doi: 10.1177/1464420719882458

41. Park SA, Lee SH, Kim WD. Fabrication of porous polycaprolactone/hydroxyapatite (PCL/HA) blend scaffolds using a 3D plotting system for bone tissue engineering. *Bioprocess Biosyst Eng*. 2011;34(4):505-513. doi: 10.1007/s00449-010-0499-2

42. Prakash C, Singh G, Singh S, et al. Mechanical reliability and in vitro bioactivity of 3D-printed porous polylactic acid-hydroxyapatite scaffold. *J Mater Eng Perform*. 2021;30(7):4946-4956. doi: 10.1007/s11665-021-05566-x

43. Ho-Shui-Ling A, Bolander J, Rustom LE, Amy Wagoner Johnson 4, Luyten FP, Picart C. Bone regeneration strategies: Engineered scaffolds, bioactive molecules and stem cells current stage and future perspectives. *Biomaterials*. 2018;180(1):143-162. doi: 10.1016/j.biomaterials.2018.07.017

44. Garot C, Bettega G, Picart C. Additive manufacturing of material scaffolds for bone regeneration: Toward application in the clinics. *Adv Funct Mater*. 2021;31(5):2006967. doi: https://doi.org/10.1002/adfm.202006967

45. Eltom A, Zhong G, Muhammad A. Scaffold techniques and designs in tissue engineering functions and purposes: A review. *Adv Mater Sci Eng*. 2019;(1):1-13. doi: 10.1155/2019/3429527

46. Choi WJ, Hwang KS, Kwon HJ, et al. Rapid development of dual porous poly(lactic acid) foam using fused deposition modeling (FDM) 3D printing for medical scaffold application. *Mater Sci Eng C*. 2020;110(1) 1-9. doi: 10.1016/j.msec.2020.110693

47. Backes EH, Fernandes EM, Diogo GS, et al. Engineering 3D printed bioactive composite scaffolds based on the combination of aliphatic polyester and calcium phosphates for bone tissue regeneration. *Mater Sci Eng C*. 2021;122(111928):1-13. doi: 10.1016/j.msec.2021.111928

48. Ribeiro JFM, Oliveira SM, Alves JL, et al. Structural monitoring and modeling of the mechanical deformation of three-dimensional printed poly(ε-caprolactone) scaffolds. *Biofabrication*. 2017;9(2):025015. doi: 10.1088/1758-5090/aa698e

49. Ye X, Zhang Y, Liu T, et al. Beta-tricalcium phosphate enhanced mechanical and biological properties of 3D-printed polyhydroxyalkanoates scaffold for bone tissue engineering. *Int J Biol Macromol*. 2022;209(1):1553-1561. doi: 10.1016/j.ijbiomac.2022.04.056

50. Sa'ude N, Kamarudin K, Ibrahim M, Irwan Ibrahim MH. *Melt Flow Index of Recycle ABS for Fused Deposition Modeling (FDM) Filament*. Trans Tech Publ. 2015.

51. Aumnate C, Pongwisuthiruchte A, Pattananuwat P, Potiyaraj P. Fabrication of ABS/graphene oxide composite filament for fused filament fabrication (FFF) 3D printing. *Adv Mater Sci Eng*. 2018;(1):1-9. doi: 10.1155/2018/2830437

52. Ang KC, Leong KF, Chua CK, Margam C. Investigation of the mechanical properties and porosity relationships in fused deposition modelling-fabricated porous structures. *Rapid Prototyp J*. 2006;1(1):1-6.

53. Ivorra-Martinez J, Peydro MÁ, Gomez-Caturla J, Sanchez-Nacher L, Boronat T, Balart R. The effects of processing parameters on mechanical properties of 3D-printed polyhydroxyalkanoates parts. *Virtual Phys Prototyp*. 2023;18(1):e2164734. doi: 10.1080/17452759.2022.2164734

54. Nugroho A, Ardiansyah R, Rusita L, Larasati IL. *Effect of Layer Thickness on Flexural Properties of PLA (PolyLactic Acid) by 3D Printing*. IOP Publishing. 2018.

55. Mahmood H, Pegoretti A, Brusa RS, Ceccato R. Molecular transport through 3-hydroxybutyrate co-3-hydroxyhexanoate biopolymer films with dispersed graphene oxide nanoparticles: Gas barrier, structural and mechanical properties. *Polym Test*.2020;81(1):1-9. doi: 10.1016/j.polymertesting.2019.106181

56. Loh QL, Choong C. Three-dimensional scaffolds for tissue engineering applications: Role of porosity and pore size. *Tissue Eng B Rev*. 2013;19(6):485-502. doi: 10.1089/ten.teb.2012.0437

57. Monshi M, Esmaeili S, Kolooshani A, Moghadas BK, Saber-Samandari S, Khandan A. A novel three-dimensional printing of electroconductive scaffolds for bone cancer therapy application. *Nanomed J*. 2020;7(2):138-148.

58. Ivorra-Martinez J, Quiles-Carrillo L, Boronat T, Torres-Giner S, A José. Covas. Assessment of the mechanical and thermal properties of injection-molded poly(3-hydroxybutyrate-co-3-hydroxyhexanoate)/hydroxyapatite nanoparticles parts for use in bone tissue engineering. *Polymers*. 2020;12(6) 1-21. doi: 10.3390/polym12061389

59. Bordes P, Pollet E, Bourbigot S, Avérous L. Structure and properties of PHA/clay nano-biocomposites prepared by melt intercalation. *Macromol Chem Phys*. 2008;209(14):1473-1484. doi: 10.1002/macp.200800022

60. Chacón JM, Caminero MA, García-Plaza E, Núñez PJ. Additive manufacturing of PLA structures using fused

deposition modelling: Effect of process parameters on mechanical properties and their optimal selection. *Mater Design*. 2017;124(1):143-157.
doi: 10.1016/j.matdes.2017.03.065

61. Kiendl J, Gao C. Controlling toughness and strength of FDM 3D-printed PLA components through the raster layup. *Compos B Eng*. 2020;180(1):1-6.
doi: 10.1016/j.compositesb.2019.107562

62. Zhou M, Zhou X, Si L, Chen P. Modeling of bonding strength for fused filament fabrication considering bonding interface evolution and molecular diffusion. *J Manuf Process*. 2021;68(1):1485-1494.
doi: 10.1016/j.jmapro.2021.06.064

63. Santo J, Penumakala PK, Adusumalli RB. Mechanical and electrical properties of three-dimensional printed polylactic acid–graphene–carbon nanofiber composites. *Polym Compos*. 2021;42(7):3231-3242.
doi: 10.1002/pc.26053

64. Singh S, Singh G, Prakash C, Ramakrishna S. Current status and future directions of fused filament fabrication. *J Manuf Process*. 2020;55(1):288-306.
doi: 10.1016/j.jmapro.2020.04.049

65. Ecker JV, Haider A, Burzic I, Huber A, Eder G, Hild S. Mechanical properties and water absorption behavior of PLA and PLA/wood composites prepared by 3D printing and injection moulding. *Rapid Prototyp J*. 2019;25(4):672-678.
doi: 10.1108/RPJ-06-2018-0149

66. Cisneros-López EO, Pal AK, Rodriguez AU, et al. Recycled poly(lactic acid)–based 3D printed sustainable biocomposites: A comparative study with injection molding. *Mater Today Sustain*. 2020;7-8(1):1-12.
doi: 10.1016/j.mtsust.2019.100027

67. Lay M, Thajudin NLN, Hamid ZAA, Rusli A. Comparison of physical and mechanical properties of PLA, ABS and nylon 6 fabricated using fused deposition modeling and injection molding. *Compos B Eng*. 2019;176(1):107341.
doi: 10.1016/j.compositesb.2019.107341

68. Komal UK, Kasaudhan BK, Singh I. Comparative performance analysis of polylactic acid parts fabricated by 3D printing and injection molding. *J Mater Eng Perform*. 2021;30(9):6522-6528.
doi: 10.1007/s11665-021-05889-9

69. Xu H, Xie L, Hakkarainen M. Beyond a model of polymer processing-triggered shear: Reconciling shish-kebab formation and control of chain degradation in sheared poly(l-lactic acid). *ACS Sustain Chem Eng*. 2015;3(7):1443-1452.
doi: 10.1021/acssuschemeng.5b00320

70. Farrag Y, Barral L, Gualillo O, et al. Effect of different plasticizers on thermal, crystalline, and permeability properties of poly(3–hydroxybutyrate–co–3–hydroxyhexanoate) films. *Polymers*. 2022;14(17):1-14.
doi: 10.3390/polym14173503

71. Watai JS, Calvão PS, Rigolin TR, do Prado Bettini SH, Souza AMC. Retardation effect of nanohydroxyapatite on the hydrolytic degradation of poly (lactic acid). *Polym Eng Sci*. 2020;60(9):2152-2162.
doi: 10.1002/pen.25459

72. Garcia Gonçalves LM, Rigolin TR, Frenhe BM, Bettini SHP. On the recycling of a biodegradable polymer: Multiple extrusion of poly (lactic acid). *Mater Res*. 2020;23(5):1-7.
doi: 10.1590/1980-5373-MR-2020-0274

73. Chaitanya S, Singh I, Song JI. Recyclability analysis of PLA/sisal fiber biocomposites. *Compos B Eng*. 2019;173(1):1-9.
doi: 10.1016/j.compositesb.2019.05.106

74. Touati N, Kaci M, Bruzaud S, Grohens Y. The effects of reprocessing cycles on the structure and properties of isotactic polypropylene/cloisite 15A nanocomposites. *Polym Degrad Stab*. 2011;96(6):1064-1073.
doi: 10.1016/j.polymdegradstab.2011.03.015

75. Agüero A, Morcillo MC, Quiles-Carrillo L, et al. Study of the influence of the reprocessing cycles on the final properties of polylactide pieces obtained by injection molding. *Polymers*. 2019;11(12):1-21.
doi: 10.3390/polym11121908

76. Majerczak K, Wadkin-Snaith D, Magueijo V, Mulheran P, Liggat J, Johnston K. Polyhydroxybutyrate: A review of experimental and simulation studies of the effect of fillers on crystallinity and mechanical properties. *Polym Int*. 2022;71(12):1398-1408.
doi: 10.1002/pi.6402

77. Trakoolwannachai V, Kheolamai P, Ummartyotin S. Characterization of hydroxyapatite from eggshell waste and polycaprolactone (PCL) composite for scaffold material. *Compos B Eng*. 2019;173(1):1-7.
doi: 10.1016/j.compositesb.2019.106974

78. Martín-Alfonso JE, Franco JM. Influence of polymer reprocessing cycles on the microstructure and rheological behavior of polypropylene/mineral oil oleogels. *Polym Test*. 2015;45(1):12-19.
doi: 10.1016/j.polymertesting.2015.04.016

79. Dhar P, Tarafder D, Kumar A, Katiyar V. Effect of cellulose nanocrystal polymorphs on mechanical, barrier and thermal properties of poly(lactic acid) based bionanocomposites. *RSC Adv*. 2015;5(74):60426-60440.
doi: 10.1039/c5ra06840a

80. Wang S, Chen W, Xiang H, Yang J, Zhou Z, Zhu M. Modification and potential application of short-chain-length polyhydroxyalkanoate (SCL-PHA). *Polymers*. 2016;8(8):1-28.
doi: 10.3390/polym8080273

81. Thomas S, Sarathchandran C, Chandran N. *Rheology of Polymer Blends and Nanocomposites: Theory, Modelling and Applications*. Elsevier. 2019.

82. Arrigo R, Bartoli M, Malucelli G. Poly(lactic acid)-biochar biocomposites: Effect of processing and filler content on

rheological, thermal, and mechanical properties. *Polymers*. 2020;12(4) 1-13.
doi: 10.3390/POLYM12040892

83. Mantia FPL, Morreale M, Scaffaro R, Tulone S. Rheological and mechanical behavior of LDPE/calcium carbonate nanocomposites and microcomposites. *J Appl Polym Sci*. 2013;127(4):2544-2552.
doi: 10.1002/app.37875

84. Petrucci R, Torre L. Filled polymer composites, In: *Modification of Polymer Properties*. 2017;Elsevier, 23-46.

85. Vaezi M, Yang S. Extrusion-based additive manufacturing of PEEK for biomedical applications. *Virtual Phys Prototyp*. 2015;10(3):123-135.
doi: 10.1080/17452759.2015.1097053

86. Jiang W, Shi J, Li W, Sun K. Morphology, wettability, and mechanical properties of polycaprolactone/hydroxyapatite composite scaffolds with interconnected pore structures fabricated by a mini-deposition system. *Polym Eng Sci*. 2012;52(11):2396-2402.

87. Fukushima K, Tabuani D, Dottori M, Armentano I, Kenny JM, Camino G. Effect of temperature and nanoparticle type on hydrolytic degradation of poly(lactic acid) nanocomposites. *Polym Degrad Stab*. 2011;96(12):2120-2129.
doi: 10.1016/j.polymdegradstab.2011.09.018

88. Sultana N, Khan TH. *In vitro* degradation of PHBV scaffolds and nHA/PHBV composite scaffolds containing hydroxyapatite nanoparticles for bone tissue engineering. *J Nanomater*. 2012;(1):1-13.
doi: 10.1155/2012/190950

89. Kim YA, Chun SY, Park SB, et al. Scaffold-supported extracellular matrices preserved by magnesium hydroxide nanoparticles for renal tissue regeneration. *Biomater Sci*. 2020;8(19):5427-5440.
doi: 10.1039/d0bm00871k

90. Jurak M, Wiącek AE, Ładniak A, Przykaza K, Szafran K. What affects the biocompatibility of polymers? *Adv Colloid Interface Sci*. 2021;294(1):1-15.
doi: 10.1016/j.cis.2021.102451

91. Wang W, Zhang B, Li M, Li J. 3D printing of PLA/n-HA composite scaffolds with customized mechanical properties and biological functions for bone tissue engineering. *Compos B Eng*. 2021;224(1):1-12.
doi: 10.1016/j.compositesb.2021.109192

92. Pachekoski WM, Dalmolin C, Agnelli JAM. The influence of the industrial processing on the degradation of poly(hidroxybutyrate)—PHB. *Mater Res*. 2013;16(2): 327-332.
doi: 10.1590/S1516-14392012005000180

93. Laput O, Vasenina I, Salvadori MC, Savkin KP. Low-temperature plasma treatment of polylactic acid and PLA/HA composite material. *J Mater Sci*. 2019;54(17): 11726-11738.
doi: 10.1007/s10853-019-03693-4

94. Gómez-Cerezo MN, Lozano D, Arcos D, Vallet-Regí M, Vaquette C. The effect of biomimetic mineralization of 3D-printed mesoporous bioglass scaffolds on physical properties and in vitro osteogenicity. *Mater Sci Eng C*. 2020;109(1):1-11.
doi: 10.1016/j.msec.2019.110572